Probing Depth-Dependent Transition-Metal Redox of Lithium Nickel, Manganese, and Cobalt Oxides in Li-Ion Batteries

Yang Yu,* Pinar Karayaylali, Livia Giordano, Juan Corchado-García, Jonathan Hwang, Dimosthenis Sokaras, Filippo Maglia, Roland Jung, Forrest S. Gittleson, and Yang Shao-Horn*

ABSTRACT: Layered lithium nickel, manganese, and cobalt oxides (NMC) are among the most promising commercial positive electrodes in the past decades. Understanding the detailed surface and bulk redox processes of Ni-rich NMC can provide useful insights into material design options to boost reversible capacity and cycle life. Both hard X-ray absorption (XAS) of metal K-edges and soft XAS of metal L-edges collected from charged $LiNi_{0.6}Mn_{0.2}Co_{0.2}O_2$ (NMC622) and $LiNi_{0.8}Mn_{0.1}Co_{0.1}O_2$ (NMC811) showed that the charge capacity up to removing ~0.7 Li/f.u. was accompanied with Ni oxidation in bulk and near the surface (up to 100 nm). Of significance to note is that nickel oxidation is primarily responsible for the charge capacity of NMC622 and 811 up to similar lithium removal (~0.7 Li/f.u.) albeit charged to different potentials, beyond which was followed by Ni reduction near the surface (up to 100 nm) due to oxygen release and electrolyte parasitic reactions. This observation points toward several new strategies to enhance reversible redox capacities of Ni-rich and/or Co-free electrodes for high-energy Li-ion batteries.

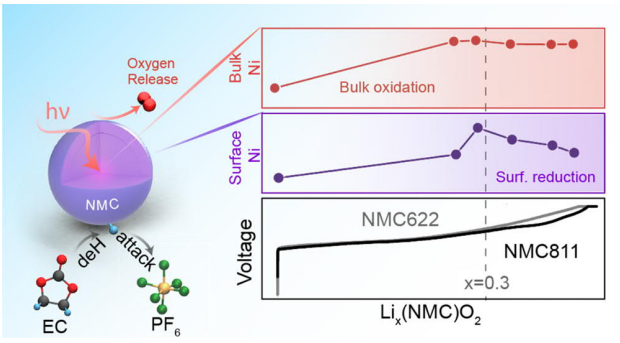

KEYWORDS: *Li-ion batteries, electrode−electrolyte interface, Ni-rich positive electrodes, NMC, X-ray absorption spectroscopy, depth-dependent redox*

1. INTRODUCTION

$LiNi_xMn_yCo_{1-x-y}O_2$ (NMC) materials are intensely studied positive electrode materials for Li-ion batteries in the past decades.[1−3] By increasing the Ni content in the NMC series from $LiNi_{1/3}Mn_{1/3}Co_{1/3}O_2$ (NMC111) to Ni-rich NMCs including $LiNi_{0.6}Mn_{0.2}Co_{0.2}O_2$ (NMC622) and $LiNi_{0.8}Mn_{0.1}Co_{0.1}O_2$ (NMC811), the discharge capacity can be greatly increased to more than 180 mAh/g at cutoff voltages of 4.3 V_{Li} and above.[2−4] However, the enhanced capacity associated with enriching Ni in NMCs[2,3,5] is accompanied with reduced capacity retention[2−7] and lower onset potential[3,4] of O_2 and CO_2 evolution upon charging. The decreased cycling stability of NMCs[3−5] has been partially attributed to increased oxidation[5,8] of carbonate solvents in the electrolyte, specifically the dissociative adsorption of carbonate solvents on surface oxygen sites of NMC to produce protic species,[5,7,9] which is associated with greater metal−oxygen covalency in NMC[10−12] at given amounts of lithium removal.[10,12] Moreover, increased O_2 loss from Ni-rich NMCs has also been correlated with a more significant capacity loss of Ni-rich NMCs over cycling. However, ambiguities still exist in the details of metal redox in these Ni-rich NMCs regarding when O_2 loss commences upon charging to high voltages, which limits the rational design of stable high-energy positive electrode materials.

X-ray absorption spectroscopy (XAS)[13−18] and electron energy loss spectroscopy (EELS)[14,19,20] have been used for revealing depth-dependent redox and structural evolution of positive electrode materials.[13−20] Tian et al.[14] have used oxygen K-edge and transition-metal L-edge soft XAS measurements, which collect the information within 100 nm from the surface, to show that nickel is oxidized consistently upon charging NMC622 to 4.6 V_{Li} (removal of ~0.7−0.8 Li/f.u.), accompanied with minimal oxidation of Co and Mn. These results are in agreement with the observation that no depth-dependent change is noted for EELS spectra of transition metals of charged NMC622 near the surface to 4.7 V_{Li} after 50 cycles (<20 nm).[14] Similarly, Kondrakov et al.[15] have combined hard X-ray (depth resolution of a few microns) and soft X-ray (depth resolution of 100 nm) adsorption spectroscopy of charged NMC811 to show continuous oxidation of Ni on the surface and in bulk up to 4.6 V_{Li}

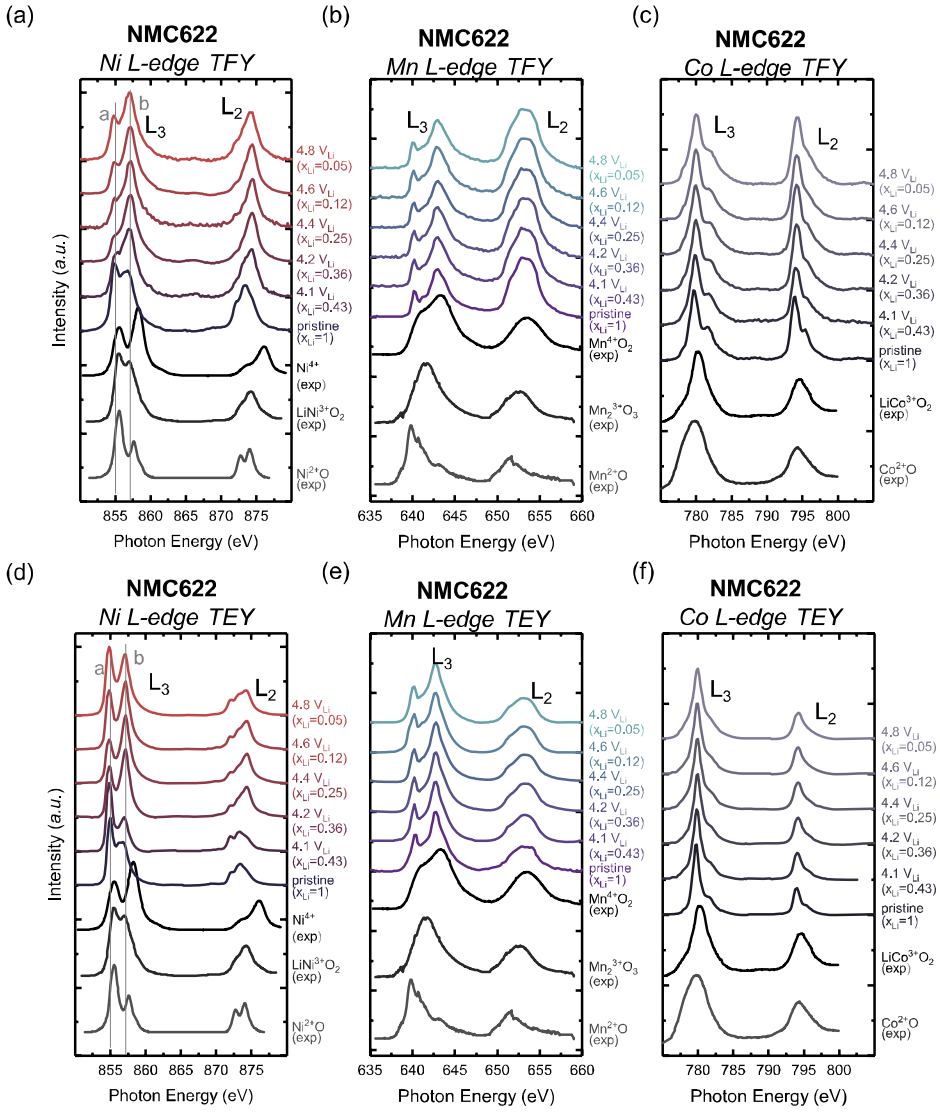

Figure 1. (a) Ni L-edge, (b) Mn L-edge, and (c) Co L-edge XAS of pristine and charged $Li_xNi_{0.6}Mn_{0.2}Co_{0.2}O_2$ (NMC622) to 4.1, 4.2, 4.4, 4.6, and 4.8 V_{Li} oxide-only pellets collected at total fluorescence yield mode (TFY) with a penetration depth of around 100 nm. (d) Ni L-edge, (e) Mn L-edge, and (f) Co L-edge XAS of pristine and charged $Li_xNi_{0.6}Mn_{0.2}Co_{0.2}O_2$ (NMC622) to 4.1, 4.2, 4.4, 4.6, and 4.8 V_{Li} oxide-only pellets collected at total electron yield mode (TEY) with a penetration depth of less than 10 nm. The reference experimental spectra of $Mn^{2+}O$,[27] $Mn_2^{3+}O_3$,[27] $Mn^{4+}O_2$,[27] $Co^{2+}O$,[27] $LiCo^{3+}O_2$,[27] $Ni^{2+}O$,[23] $LiNi^{3+}O_2$,[23] and $K_2Ni^{4+}(H_2IO_6)_2$.[23] Mn L-edges and Co L-edges of charged and pristine NMC622 have minimal changes as a function of lithium contents, indicating no significant participation in the redox process, as quantified in Figure 3. Ni L-edges of NMC622 show consistent oxidation of Ni upon removing around 0.7 Li/f.u. and then experience a (sub)surface reduction, as quantified in Figure 3. The example charge profile of the pellets is shown in Figure S1. The computed reference spectra using the charge-transfer multiplet model (CTM) are shown in Figure S2.

(removal of ~0.78 Li/f.u.), where the oxidation state of Co and Mn remains largely unchanged. On the other hand, online electrochemical mass spectrometry (OEMS) measurements of O_2 loss from charged NMC622 and NMC811 to 4.4 V_{Li}[3] have allowed for thickness estimation of formed rocksalt NiO-like surface layers, with a thickness of ~10 nm for charged NMC622 and 14 nm for charged NMC811. These thickness estimations are in reasonable agreement with the observed thickness of ~6 nm of rocksalt on the surface of NMC811 cycled to 4.3 V_{Li} after 83 cycles using transmission electron microscopy (TEM).[19] It is of greater interest to understand whether the formation of these microscopically observed rocksalt layers (with much reduced oxidation state than layered compounds) due to surface O_2 loss can be probed by examining Ni oxidation state changes near the surface and in bulk by X-ray adsorption spectroscopy and how Ni oxidation changes near the surface differ with increasing Ni from NMC622 to NMC811. This understanding is critical to designing Ni-rich NMC or Co-free electrodes at high cutoff voltages for high-energy Li-ion batteries.

In this work, we employ a combination of soft and hard X-ray absorption spectroscopy (sXAS and hXAS) to probe the surface with total electron yield (TEY) with a depth resolution of <10 nm, total fluorescence yield (TFY) with a depth resolution of 100 nm,[14,16] and the bulk[15] (depth resolution >1 μm) oxidation of charged NMC622 and NMC811. We examine oxide-only electrodes that are free of carbon and binder obtained at different state-of-charge in the first cycle,

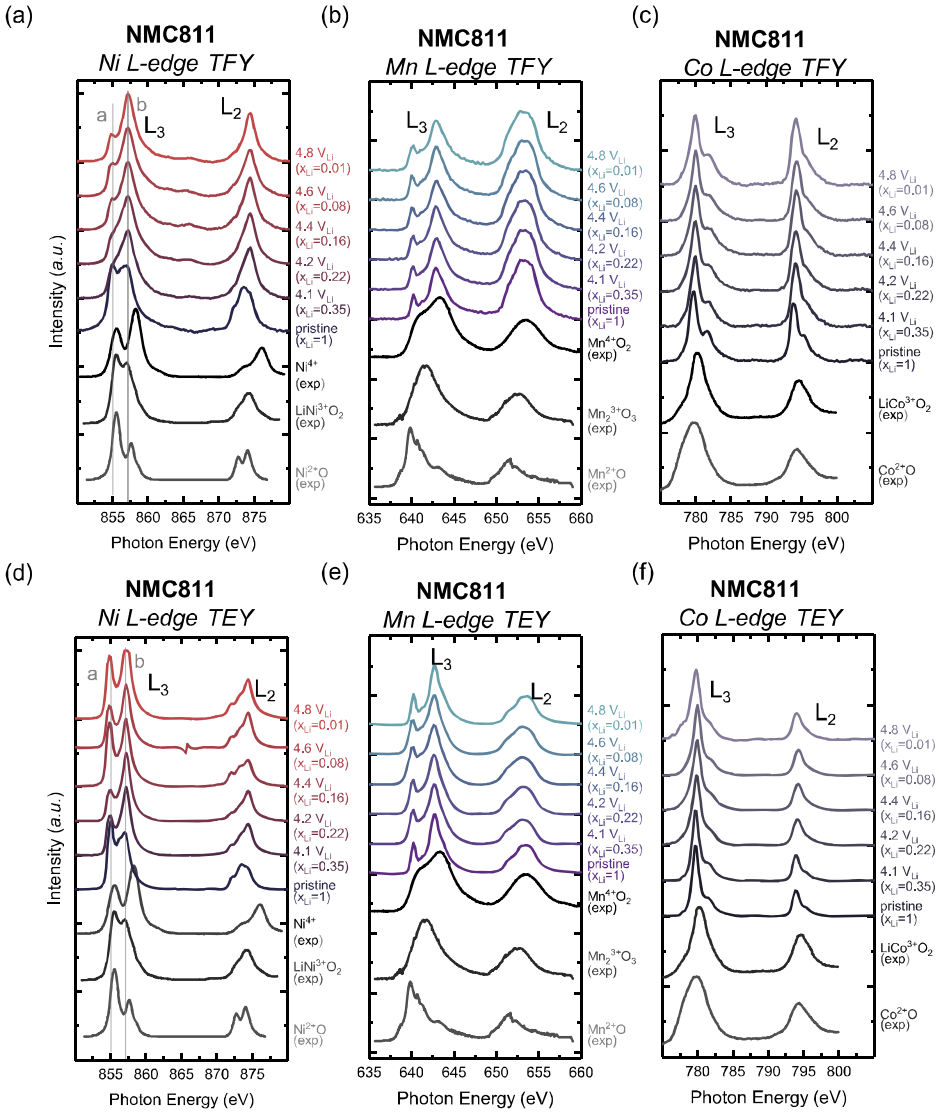

Figure 2. (a) Ni L-edge, (b) Mn L-edge, and (c) Co L-edge XAS of pristine and charged $Li_xNi_{0.8}Mn_{0.1}Co_{0.1}O_2$ (NMC811) to 4.1, 4.2, 4.4, 4.6, and 4.8 V_{Li} oxide-only pellets collected at total fluorescence yield mode (TFY) with a penetration depth of around 100 nm. (d) Ni L-edge, (e) Mn L-edge, and (f) Co L-edge XAS of pristine and charged $Li_xNi_{0.8}Mn_{0.1}Co_{0.1}O_2$ (NMC811) to 4.1, 4.2, 4.4, 4.6, and 4.8 V_{Li} oxide-only pellets collected at total electron yield mode (TEY) with a penetration depth of less than 10 nm. The reference experimental spectra and computed spectra using the charge-transfer multiplet model (CTM) of $Mn^{2+}O$,[27] $Mn_2{}^{3+}O_3$,[27] $Mn^{4+}O_2$,[27] $Co^{2+}O$,[27] $LiCo^{3+}O_2$,[27] $Ni^{2+}O$,[23] $LiNi^{3+}O_2$,[23] and $K_2Ni^{4+}(H_2IO_6)_2$.[23] Mn L-edges and Co L-edges of charged and pristine NMC811 have minimal changes as a function of lithium contents, indicating no significant participation in the redox process, as quantified in Figure 3. Ni L-edges of NMC811 show consistent oxidation of Ni upon removing around 0.7 Li/f.u. and then experience a (sub)surface reduction, as quantified in Figure 3. The example charge profile of the pellets is shown in Figure S1. The computed reference spectra using the charge-transfer multiplet model (CTM) are shown in Figure S2.

focusing primarily on the high state-of-charge compared to previous studies.[15,16] The use of the oxide-only electrode allows us to decouple the oxide redox process with the binder and carbon parasitic reaction products. sXAS, more sensitive to surface redox than hXAS, revealed that surface redox began to deviate from bulk upon charging NMC622 and NMC811 at 4.2 V_{Li} and above. By combining the oxidation state changes of metal ions from near the surface to bulk, we show that Ni near the surface and in bulk gradually become oxidized up to 4.2 V_{Li} for NMC622 and 4.1 V_{Li} for NMC811 or upon lithium removal of 0.7−0.8/f.u., beyond which is accompanied with Ni reduction in the surface regions (10 nm).

2. RESULT AND DISCUSSION

sXAS TFY and TEY measurements of metal L-edges collected from pristine and charged NMC622 (Figure 1) and NMC811 (Figure 2) pellets revealed gradual nickel oxidation upon lithium removal up to 0.7 Li/f.u. (x_{Li} = ~0.3) while no significant changes were found for cobalt and manganese. Ni, Mn, and Co L-edges of these samples are composed of two major regions (L_3 and L_2). The region at low photon energy, referred to as L_3 edge, is corresponding to the transition from $2p_{3/2}$ to unoccupied 3d states, while the other feature located at high photon energy (10−15 eV separation from the L_3 features) is referred to as L_2 edge, corresponding to the transition from $2p_{1/2}$.[21,22] As the L_3 edge of the 3d transition metal is around twice as intense compared to the L_2 edge

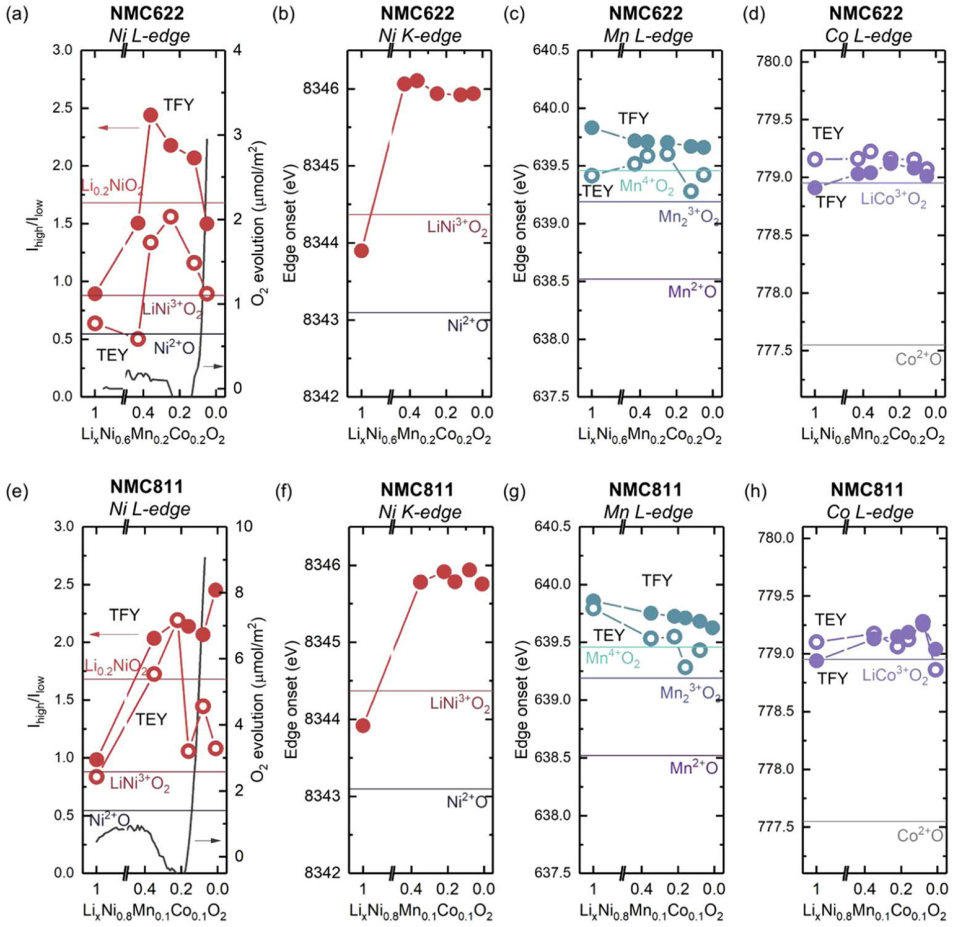

Figure 3. Quantification of the oxidation state of (a) Ni L_3-edge, (b) Ni K-edge, (c) Mn L_3-edge, and (d) Co L_3-edge XAS of pristine and charged $LiNi_{0.6}Mn_{0.2}Co_{0.2}O_2$ (NMC622) to 4.1, 4.2, 4.4, 4.6, and 4.8 V_{Li} oxide-only pellets collected at TEY (closed circle) and TFY (open circle), representing the redox process at less than 10 and 100 nm, respectively. The Ni K-edge is measured under transmission mode. (f) Ni K-edge, (g) Mn L_3-edge, and (h) Co L_3-edge XAS of pristine and charged $LiNi_{0.8}Mn_{0.1}Co_{0.1}O_2$ to 4.1, 4.2, 4.4, 4.6, and 4.8 V_{Li} oxide-only pellets collected TEY (open circle) and TFY (closed circle) (Figure 2), representing the redox process at less than 10 and 100 nm, respectively. The Ni K-edge is measured under transmission mode, representing the redox process more than 1 μm, where the raw Ni K-edge, Mn K-edge, and Co K-edge spectra are shown in Figure S5, and the quantification is shown in Figure S6. Quantification of experimental spectra of $Mn^{2+}O$,[27] $Mn_2^{3+}O_3$,[27] $Mn^{4+}O_2$,[27] $Co^{2+}O$,[27] $LiCo^{3+}O_2$,[27] $Ni^{2+}O$,[23] $LiNi^{3+}O_2$,[23] and $Li_{0.2}NiO_2$[16] is shown as lines. Oxygen evolution of NMC622 and 811 (μmol/cm$_{oxide}^2$) as a function of lithium contents from previous OEMS studies[3] is shown as gray lines.

because the occupancy ratio of the $p_{3/2}$ orbital is twice as that of $p_{1/2}$,[21] therefore we primarily analyzed changes in metal oxidation with the L_3 edge.[14,16,21] The Ni L_3-edge doublet of NMC622 (Figure 1a) and NMC811 (Figure 2a) collected in the TFY mode was found to have the high-energy peak (peak b) grow at the expense of the low-energy peak (peak a) upon charging to 4.2 V_{Li} (x_{Li} (lithium content) = 0.36) and 4.1 V_{Li} (x_{Li} = 0.35), respectively, beyond which the trend was reserved upon further lithium removal. Similar changes were found for TEY Ni L_3-edge data for NMC622 and 811. (Figures 1d and 2d) These changes are indicative of nickel oxidation up to removing ~70% of Li, which is supported by similar changes observed in reference compounds of nickel oxidation states including $Ni^{2+}O$, $LiNi^{3+}O_2$, and $K_2Ni^{4+}(H_2IO_6)_2$.[23] Further support comes from the simulated spectra using a charge-transfer multiplet model (CTM) developed by Groot et al.,[24] where increasing the oxidation state from Ni^{2+} to Ni^{3+} in an octahedral coordination is accompanied by greater intensity of the high-energy peak compared to the low-energy feature (Figure S2). Such a trend in the intensity ratio is not captured by *ab initio* based tools, for example, OCEAN,[25] which focuses on having an accurate description of density of states (DOS), as shown in Figure S3. For example, by calculating the Ni L-edges of Li_xNiO_2 (x = 1, 0.5, 0.33) using OCEAN code, there is no significant difference in the features by removing lithium, coupled with only a tiny shift in the Ni L_3-edge whiteline in the relative energy scale, indicative of potential Ni oxidation. The insensitivity of OCEAN to 3d metal L-edges lies in that for highly correlated 3d transition metals, the L-edge is overwhelmed by the exciton (electron−hole pair) effect instead of the ground-state density of states,[21] where OCEAN might be not too sensitive in capturing the exciton effect as a function of metal oxidation state. Such an observation is in contrast with a relatively accurate description of 4d metal L-edge studied in our previous work using OCEAN,[26] where 4d metal L-edges are predominantly dictated by ground-state DOS.[21] On the other hand, no noticeable changes were observed for Mn (Figures 1b,e and 2b,e) and Co (Figures 1c,f and 2c,f) L-edges of charged NMC622 and NMC811, suggesting insignificant changes in their oxidation states upon charging the oxides.

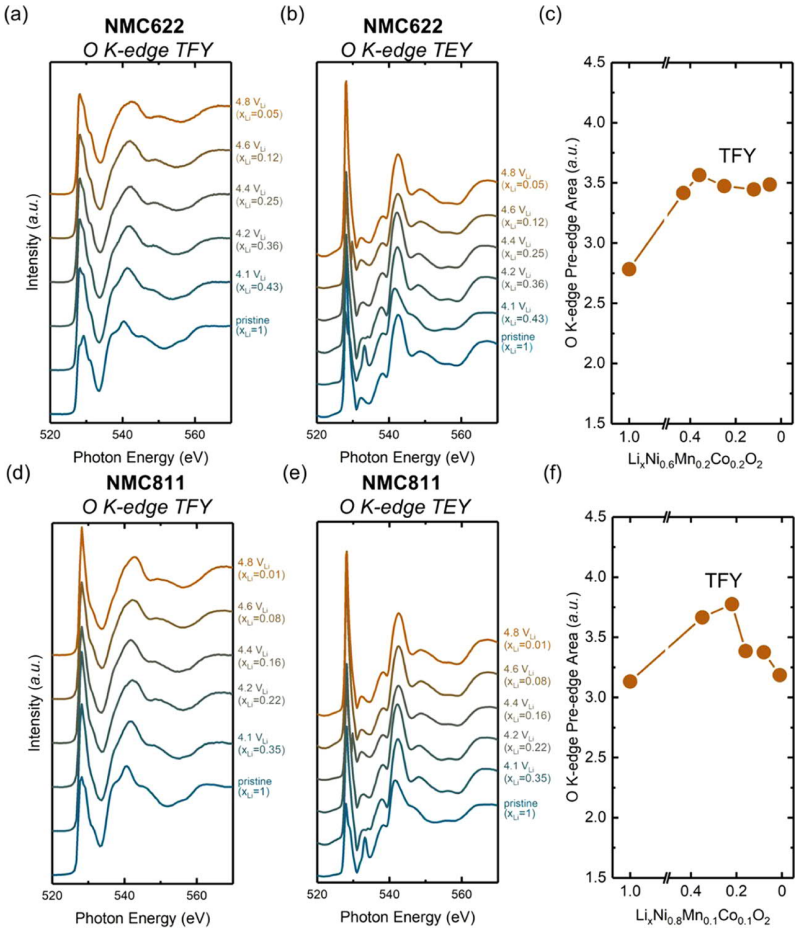

Figure 4. O K-edge sXAS of (a) TFY and (b) TEY of pristine and charged $LiNi_{0.6}Mn_{0.2}Co_{0.2}O_2$ (NMC622) to 4.1, 4.2, 4.4, 4.6, and 4.8 V_{Li} oxide-only pellets, where the quantification of the pre-edge area of O K-edge TFY is shown in (c). O K-edge sXAS of (d) TFY and (e) TEY of pristine and charged $LiNi_{0.8}Mn_{0.1}Co_{0.1}O_2$ (NMC811) to 4.1, 4.2, 4.4, 4.6, and 4.8 V_{Li} oxide-only pellets, where the quantification of the pre-edge area of O K-edge TFY is shown in (f). It was shown that for NMC622 and NMC811, the prepeak area increases as a function of voltage upon charging to 4.2 V_{Li} (lithium removal 0.7−0.8 Li/f.u.), indicating transition-metal oxidation upon charging followed by a prepeak area decrease with further lithium removal, which is matching with the sXAS Ni L-edge shown in Figure 3. The quantification of the prepeak area in TEY is shown in Figure S7.

2.1. sXAS TFY and TEY Ni-L_3 and O-K-Edge Measurements of Charged NMC622 and NMC811. The ratio of high-energy to low-energy peak intensity in the Ni L_3 doublet of TFY and TEY data was quantified to show the trends in the oxidation state of transition metal in charged NMC622 and NMC811 (Figure 3a,3e). It should be noted that these trends found for TFY and TEY data are not dependent on the methods of analyzing the oxidation state, where by using centroid position to extract the oxidation state in Figure S4a,d, we observe similar trends. The peak intensity ratio of pristine NMC622 (Figure 3a) and NMC811 (Figure 3e) in the TFY mode is close to that of $LiNiO_2$, indicative of a nickel oxidation state of ∼3+. The peak intensity ratio of Ni TFY L_3 collected from charged NMC622 and charged NMC811 was found to increase up to 4.2 V_{Li} (lithium removal of ∼0.66 Li/f.u (x_{Li} = ∼0.34), Figure 3a) and 4.1 V_{Li} (lithium removal of ∼0.65 Li/f.u (x_{Li} = ∼0.35), Figure 3e), respectively, indicating nickel oxidation in regions 100 nm below the surface. Further Li removal is accompanied with the reduction in the TFY L_3 peak intensity of charged NMC622 and peak intensity flattening of charged NMC811. Further insights to nickel oxidation state changes came from TFY oxygen K-edge sXAS measurements of charged NMC622 and NMC811 pellets (Figure 4). The prepeak area of oxygen K-edge TFY (Figure 4c,f) for charged NMC622 and NMC811 was found to first increase upon charging to 4.2 and 4.1 V_{Li}, respectively. As greater prepeak area of oxygen K-edge indicates more unoccupied states for TM 3d − O 2p states[28,29] and greater Ni−O covalency, increasing the prepeak area of charged NMC622 and NMC811 further supports the oxidation of Ni, in agreement with Ni TFY L_3 measurements. Flattened prepeak area of oxygen K-edge TFY (Figure 4c,f) for charged NMC622 upon further Li removal suggests no significant nickel reduction or oxygen loss within regions 100 nm from the surface. This argument is supported by the amount of oxygen evolution detected in the previous OEMS measurements.[3] Considering oxygen evolution only from previous OEMS measurements[3] of charged NMC622 would only translate to negligible nickel reduction (a valence change of 0.007), where we assume oxygen loss from regions within 100 nm of the surface and an average primary particle size of 7 μm based on the microscopy images from previous work[8] (Supporting Information Notes 1 and 2). However, the reduction in the ratio of high-energy to low-energy peak intensity in the TFY Ni L_3 doublet of charged NMC622 beyond lithium removal of ∼0.66 Li/f.u. (x_{Li} = ∼0.34) (Figure 3a), which is accompanied with the shift of the

TFY Ni L_3 peak centroid (Figure S4) toward lower photon energy, is not well understood, which can be the result from increasing redox contributions from other metal centers other than Ni. For example, at low state-of-charge, slight Co oxidation was observed in Co L-edge TFY (Figure 3d), which was accompanied with more covalent interaction between Co−O, resulting in a less covalent interaction between Ni−O and Mn−O due to the inductive effect.[30] This argument may explain the reduction of Ni effective charges upon further charge, requiring future studies. Therefore, combining the TFY and previous OEMS results suggests that charged NMC622 has no considerable oxygen loss and nickel reduction within regions 100 nm from the surface with lithium removal beyond ∼0.8 Li/f.u. (x_{Li} = ∼0.2). In contrast, the prepeak area of oxygen K-edge TFY (Figure 4c,f) for charged NMC811 was found to decrease significantly upon charging to voltages greater than 4.1 V_{Li} (Figure 4f), indicating considerable metal reduction within regions 100 nm from the surface. Such nickel reduction of charged NMC811, observed mostly pronouncedly at lithium removal of ∼0.8 Li/f.u. (x_{Li} = ∼0.2), can be attributed to oxygen loss from oxide lattice, as reported by previous OEMS[3] and differential electrochemical mass spectrometry (DEMS) measurements.[31−33] Oxygen loss detected from previous OEMS measurements[3] of charged NMC811 would translate to some nickel reduction (Ni valence reduction of 0.07) upon lithium removal beyond ∼0.8 Li/f.u. (x_{Li} = ∼0.2) within regions 100 nm from the surface (Supporting Information Note 2), and by attributing all of CO_2 evolution from lattice oxygen, it results in a Ni valence reduction of 2. Therefore, TFY Ni-L_3 and O-K measurements with previous OEMS results suggests that charged NMC811 has considerable oxygen loss from the oxide lattice and nickel reduction with lithium removal beyond ∼0.8 Li/f.u. (x_{Li} = ∼0.2) within regions 100 nm from the surface. Moreover, by combining with the previous DEMS result, some of the oxygen loss could attribute to the CO_2 evolution during first charge.[3,4]

We further compare Ni L_3 TEY data (probing 10 nm from the surface) with those of TFY (probing 100 nm from the surface) for charged NMC622 and NMC811. The ratio of high-energy to low-energy peak intensity in the Ni L_3 doublet of TEY data (10 nm) collected from pristine NMC622 (Figure 3a) and NMC811 (Figure 3e) was found lower than that of TFY, indicating regions 10 nm from the surface more reduced than regions 100 nm below the surface, which is commonly observed in transition-metal oxides.[14,17,34,35] Ni reduction on the surface of pristine NMC622 and NMC811 can be attributed to the formation of surface metal carbonate and/or hydroxyl formation during synthesis and storage in the Ni-rich positive electrode.[36] The formation of Ni and/or Li carbonate is further supported by the O K-edge TEY sXAS data of pristine oxide-only pellets (Figure 4), as indicated by the characteristic peak around 532−533 eV[37] of carbonates. The ratio of high-energy to low-energy peak intensity in the TEY Ni L_3 doublet of charged NMC622 (Figure 3a) was shown to follow a similar trend to that of TFY (Figure 3a) but with lowered values. These observations suggest that upon charging Ni oxidation state evolution in regions 10 nm from the surface regions traced that observed in 100 nm from the surface but was more reduced. On the other hand, not only the TEY data of charged NMC811 traced the trend of TFY data (Figure 3e), but also the ratio of TEY Ni L_3 data of charged NMC811 (Figure 3e) was close to that of TFY data upon charging to 4.2 V_{Li}, suggesting that NMC811 surface is less reactive compared to NMC622 at low state-of-charge. These results suggest that regions in ∼10 nm from the surface have similar nickel oxidation to bulk upon charging up to 4.2 V_{Li} and become more reduced at a higher state-of-charge. The decreased intensity ratio from the TEY data for charged NMC622 (Figure 3a) and NMC811 (Figure 3e) beyond lithium removal of 0.7 Li/f.u.(x_{Li} = ∼0.3) could be attributed to the formation of more reduced nickel species such as NiO on the surface, resulting from surface oxygen release and dissociative adsorption of carbonate solvents on surface oxygen sites to reduce the transition metal.[5,9] Unfortunately, further examination of TEY O K-edge sXAS data of charged NMC622 and NMC811 (Figures 4b,e and S7) revealed no further insights due to lack of systematic trends with Li removal, suggesting potentially greater influence from the formation of oxygenated electrolyte decomposition products on the surface compared to metal L-edges. From our previous work,[5] we have shown that the electrode−electrolyte interface is limited to a thickness of less than 10 nm due to the presence of obvious lattice oxygen signal in the charged NMC from XPS O1s spectra, therefore O K-edge XAS TEY could be largely affected by the electrolyte decomposition parasitic products deposited on the surface. Finally, the amounts of Li removal for the onset of Ni reduction for regions 10 nm from the surface shown from TEY measurements of charged NMC622 and NMC811 as well as charged $LiNiO_2$[16] are comparable (∼0.7 Li/f.u (x_{Li} = ∼0.3)) and independent of the bulk Ni content. This observation of this surface Ni reduction onset is comparable to the observed onset voltages of oxygen release from charged NMC622 and NMC811 reported from previous literature.[3,4,31,32] Much lower Ni oxidation state from NMC622 charged to 4.8 V_{Li} compared to NMC811 charged to that voltage is contradictory with more reactive NMC811 surface. Such discrepancies could be reconciled by the very comparable oxygen evolution amount at 4.8 and 5.0 V_{Li} from previous OEMS measurements.[3] Moreover, due to the difference in the electronic structures of NMC622 and 811 and the Ni L-edge doublet ratio, quantitative comparison across these two different chemistries might not be very rigorous. Further investigation using X-ray microscopy[38] should be employed to understand the spatial distribution and morphology of the oxide particles charged to such high potentials. It is worthy to note, even though we have included the literature data of the intensity ratio of Ni doublet for different Ni oxidation states in Figure 3 to qualitatively compare the oxidation state of charged NMC with the experimental reference, we did not extract the exact nominal oxidation state of our samples because such comparison requires corrections of the incident beam dynamics and the quantum efficiency of the detectors for both the literature data and the measurements in this work. We reported the experimental reference for the doublet peak ratio just for a comparison with previous work on $LiNiO_2$-derived systems.[14,16,17]

2.2. Connecting Ni sXAS With hXAS Measurements of Charged NMC622 and NMC811. Ni K-edge energy collected from charged NMC622 and NMC811 (depth penetration greater than 1 μm,[39] Figures 3b,f and S5a,d) was found to shift positively upon charging to 4.2 and 4.1 V_{Li}, respectively, beyond which minimal change was observed. Metal K-edge raw spectra comprise one major peak (Figure S5), corresponding to the transition from 1s to 4p,[40] and a minor feature at 15 eV lower photon energy, corresponding to 1s to 3d transition state that is theoretically dipole-forbidden

but quadrupole allowed due to slight M-O octahedron distortion.[40] The Ni K-edge of charged NMC622 to 4.2 V_{Li} (Figures 3b and S5a) and NMC811 to 4.1 V_{Li} (Figures 3f and S5d) was shifted significantly to higher photon energy. In addition, the Ni K-edge shift is accompanied with shortened Ni−O bond length (∼1.97 to ∼1.89 Å) fitted from Extended X-ray absorption fine structure (EXAFS) analysis of NMC622 (Figures S8a, S9, and S11a) and NMC811 (Figures S8b, S10, and S11b). These observations indicate upon charging to 4.1 V_{Li}, nickel oxidation largely happens in bulk, in agreement with previous studies of sXAS and hXAS.[15] Further charging to higher voltages (lithium removal beyond ∼0.6 Li/f.u.) resulted in minimal change observed in bulk coming from Ni K-edge spectra of charged NMC622 (Figure 3b) and NMC811 (Figure 3f). Different from the observation near the surface, further removing more than ∼0.7 Li/f.u. (x_{Li} = ∼0.3) results in no noticeable further oxidation in the Ni K-edge data of charged NMC622 and NMC811 (Figures 3b,f and S5a,d) as well as no further reduction in the Ni−O bond length from the EXAFS spectra (Figures S11,S12). Similar observations in the Ni−O bond length have been noted for charged Li-$Ni_{0.85}Co_{0.15}O_2$, where the Ni−O bond length was stabilized at ∼1.89 Å by removing ∼0.6 Li/f.u. (x_{Li} = ∼0.4) and more (Figure S13). Therefore, Ni K-edge hXAS combined with Ni L-edge and O K-edge sXAS shows bulk and surface nickel oxidation upon lithium removal up to ∼0.7 Li/f.u. (x_{Li} = ∼0.3), beyond which nickel can become reduced in regions 10 nm from the surface due to oxygen release and dissociative adsorption of carbonate solvents on surface oxygen sites to reduce the transition metal.[5,9]

2.3. sXAS and hXAS Measurements of Mn and Co on Charged NMC622 and NMC811. Unlike Ni, Co, and Mn in charged NMC622 and NMC811 exhibit small changes upon lithium removal from sXAS measurements. The doublet feature of TFY and TEY Mn L_3 edge of charged NMC622 (Figure 1b,e) and NMC811 (Figure 2b,e) is indicative of Mn^{4+}, which is supported by the reference spectra used in this study, simulated spectra from CTM (Figure S2) and previous studies.[41,42] Moreover, for Mn L-edges, as we increase the oxidation state of Mn in the experimental reference (Figure 1b) as well as CTM-simulated reference in Figure S2, there is an obvious shift for the spectroscopic edge toward high photon energy. It is worthy to note that the CTM model tends to have an overestimation of such shift for Mn^{4+}; this inaccuracy in photon energy is also acknowledged in the previous study on Fe-based systems.[43] Upon charging, the TFY Mn L-edge spectra of charged NMC622 and NMC811 remained largely unchanged, with a small shift of the onset edge energy to lower photon energy with increasing Li removal, indicative of slight reduction from Mn^{4+}, presumably due to the inductive effect associated with nickel oxidation. No significant changes were found for the TEY Mn L-edge energy (probing 10 nm from the surface) of charged NMC622 (Figure 3c), indicating negligible Mn reduction, up Li removal to 0.9 Li/f.u. (x_{Li} = ∼0.1). In contrast, the TFY Mn L-edge energy of charged NMC811 decreased monotonically with increasing Li removal (Figure 3g), suggesting potential subsurface Mn reduction, presumably attributable to the formation of secondary phases such as Mn spinel and/or rocksalt[20,44] on the surface. However, the significance of the observed backshift of Mn, compared to the energy resolution of 0.2 eV for 3d metal L-edge XAS, remains debatable. On the other hand, the peak feature and energy of TFY and TEY Co L_3 edge of charged NMC622 (Figure 1b,e) and NMC811 (Figure 2b,e) is indicative of Co^{3+}, which is supported by reference spectra used in this study, simulated spectra from CTM (Figure S2) and previous studies.[42] Similar to what is observed in Mn L-edge references, increased Co oxidation states in the experimental and computational references also induce an obvious positive shift in the edge and centroid. Moreover, the TFY Co L-edge spectra of charged NMC622 (Figure 1c) and NMC811 (Figure 2c) also remained largely unchanged with Li removal, having a small shift toward higher edge onset energy (Figure 3d,h) with increasing Li removal up to ∼0.9 Li/f.u. (x_{Li} = ∼0.1). This observed shift is not very significant compared to the energy resolution of spectra, which is 0.2 eV. These results suggest that Co oxidation has a small contribution to charge compensation upon lithium removal from charged NMC622 and NMC811. Negligible changes were noted for the TEY Co L-edge energy of charged NMC622 (Figure 3d) and charged NMC811 (Figure 3h), indicating no significant changes for Co oxidation in regions 10 nm from the surface, with increasing Li removal to ∼0.9 Li/f.u. (x_{Li} = ∼0.1).

Moreover, no significant changes were observed for Mn and Co K-edges of charged NMC622 and NMC811 (Figures S5 and S6), albeit there appeared to be a slight positive shift in the edge energy of Co K-edge, indicative of very slight bulk oxidation of Co in NMC811, especially upon charging to 4.4 V_{Li} and higher. Considering the nominal oxidation potential of Co in Li_xCoO_2 at ∼3.9 V_{Li},[45] Co oxidation at substantially higher voltages in charged NMC622 and NMC811 can be rationalized by the argument that Ni^{3+} has more covalent bonding with oxygen as compared to Co^{3+} in $LiCoO_2$, therefore inducing less covalent bonding between Co and oxygen due to inductive effect, lowering the antibonding states of the Co−O bond, and increasing the oxidation voltage of Co in NMC622 and NMC811.[30] This observation indicates that no matter what the substituents are, unless it is more electronegative than Ni^{3+} and redox active, introduction of those cations may not necessarily boost the redox capability of such system and will not delay the surface oxygen release onset potential/capacity.

2.4. Transition-Metal Redox of Charged NMC622 and NMC811 and Implication for Materials Design. By combining sXAS with hXAS measurements on Ni, Mn, and Co as well as sXAS on O K-edge of charged NMC622 and NMC811, we show that Ni in regions 100 nm from the surface (Figure 3a,3e) and in bulk (Figure 3b,3f) becomes oxidized upon Li removal to 0.7 Li/f.u., primarily responsible for charge compensation, where Co is slightly oxidized (Figures 3d,h, S6b, and S6d) and Mn is slightly reduced (Figures 3c,g, S6a, S6c). These changes indicate that the Ni^{3+} 3d states are above Co^{3+} 3d states, which are above Mn^{4+} 3d states, in NMC622 and NMC811. Beyond Li removal to 0.7 Li/f.u., there is no significant oxygen loss and nickel reduction in bulk and in regions 100 nm from both Ni L-edge and K-edge as well as O K-edge measurements. On the other hand, Ni cations in regions 10 nm from the surface of charged NMC622 (Figures 3a and 4c) and NMC811 (Figures 3e and 4f) become noticeably reduced upon Li removal of ∼0.7 Li/f.u. (x_{Li} = ∼0.3) and higher, which onset is independent on bulk Ni content in NMC. The onset state of charge (Li removal of 0.8/f.u. (x_{Li} = ∼0.2)) matches with previous DEMS[31−33] and OEMS measurements[3,4] on NMC622 and NMC811 as well as other Ni-based systems such as $LiNiO_2$, where oxygen release starts at state-of-charge around 80%.[16] These observation

suggests that the observed Ni reduction in regions 10 nm from the surface upon Li removal of 0.8 Li/f.u. and higher can be attributed to oxygen release from oxides as well as dissociative adsorption of carbonate solvents on surface oxygen sites to reduce the transition metal and form protic species.[5,9] The greater oxygen loss found from charged NMC811 than charged NMC622 at Li removal of ~0.8 Li/f.u. (x_{Li} = ~0.2) from previous OEMS measurements is accompanied with greater Ni reduction in regions 10 nm from the surface for charged NMC811 (Figures 3e and 4f) but minimum reduction of Co and Mn. Therefore, while Mn and Co may have stabilizing effects for Ni-rich NMC at high state-of-charge,[2,46] the redox of $Ni^{3+/4+}$ (Figure 5) is largely responsible for charge compensation in Ni-rich oxides during reversible lithium intercalation and irreversible oxygen release.

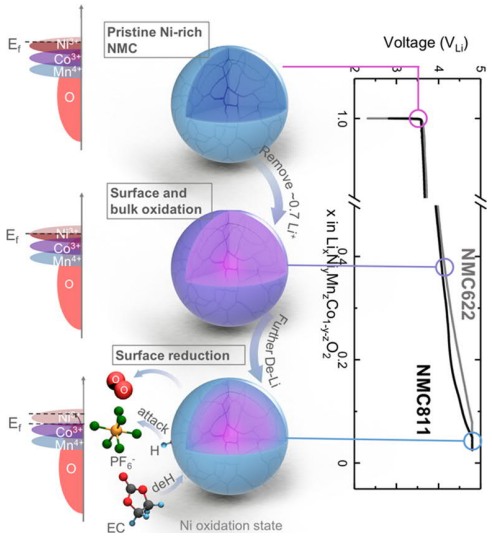

Figure 5. Schematics of the surface and bulk Ni redox process of Ni-rich NMC622 and 811 summarized from the sXAS and hXAS data shown in Figures 2, 3, and 4, where the bulk and surface of the pristine NMC experienced Ni oxidation upon charging by removing around 0.7 Li^+/f.u., coupled with depleting electrons from the metal states. This is followed by a surface Ni reduction upon further charging, coupled with oxygen release reported by previous literature, and back-filling of electrons to the Fermi level from oxygen due to oxygen vacancy creation.[3,4,31−33,47] The oxygen release is coupled with the electrolyte decomposition reactions where the carbonate solvent dissociative adsorbs on the oxide surface, reducing the transition metal, forming protic species, which could further attack the salt species.[5]

The observed metal redox process presented in this work, where the cationic capacity has limited dependence on bulk Ni content, points toward two major strategies of bulk materials design that can further push the Ni redox capacity that is eventually free of Co. The first strategy points toward cationic substitution contributing to the redox in parallel with $Ni^{2.x+/4+}$ redox, requiring similar and even slightly higher electronegativity compared to $Ni^{3+/4+}$ states. Such consideration lies in that electronegativity is directly correlated with the metal redox level, where more electronegative substituents introduce more covalent M-O interaction and lower down oxidation voltage of the substituent in comparison to Ni redox due to inductive effect.[30] This strategy points toward substitution of more delocalized and slightly more electronegative 4d and 5d transition metals in the system such as Nb^{4+}, Ru^{4+}, Rh^{4+}, Pt^{4+}, $W^{4+/5+}$, etc. Another strategy includes reducing Ni oxidation state through cationic dopants of higher oxidation state compared to oxygen. By introducing metal with a higher oxidation state than Mn^{4+}, Ni can be further reduced closer toward 2+, providing more capacity before reaching Ni^{4+} and oxygen release, for example, Nb^{5+} and W^{5+} can fulfill such purpose. Recently, W dopants are also explored by Ryu et al.[48] and showed promising performance with suppressed H2 to H3 phase transition, hinting at less degree of oxygen release. The design strategies we discussed are only targeted at improving the bulk redox capability of Ni-based oxides, yet the capacity retention in the subsequent cycles also hinges on the interfacial reactivity of the oxides toward the electrolyte. Even though in this work, we have shown minimal dependence of Ni redox process on bulk Ni content, in our previous works on interfacial reactions of Ni-rich positive electrodes toward the electrolyte, the interfacial reactivity is directly related to Ni contents and is closely related to cycling stability of the electrodes.[5,7,49] Therefore, when designing the bulk oxides, consideration on the methods to mitigate oxide reactivity toward carbonate also needs to be taken, which includes extra consideration on surface treatment and processing and storage conditions, which could have a large impact on the interfacial reactions and reversible capacities.

3. CONCLUSIONS

In this work, we combined soft and hard X-ray absorption spectroscopy to study the redox process of Ni, Mn, and Co in Ni-rich NMC. We have shown that compared to hXAS, sXAS is much more sensitive to the surface processes, which are dominating at high state-of-charge. We observed through Ni L-edge TEY and TFY, as well as O K-edge TFY, a consistent oxidation of Ni up to removing around 0.7 Li/f.u. (x_{Li} = ~0.3) in NMC622 and 811 to a nominal oxidation state of around 4+ in both bulk and surface, followed by a surface Ni reduction back to Ni^{3+}. Such reduction is only limited to the region within 10 nm from the surface, shown by stagnant bulk Ni K-edge onsets at high state-of-charge. Meanwhile, Co and Mn show minimal participation in this redox process from both hXAS and sXAS characterization. The surface Ni reduction process is the result of surface oxygen release and directly correlated with irreversible capacity in the formation cycle. The onset of this reduction matches perfectly with the observed OEMS oxygen release onset and is state-of-charge-dependent (70−80% state-of-charge), yet not bulk Ni content dependent. Through those findings, an overall depth-dependent redox mechanism is proposed for Ni-rich NMC, which provides insights in future bulk material design of Ni-based electrodes to further boost its reversible capacity.

4. METHODS

4.1. Electrode Preparation. NMC622 ($LiNi_{0.6}Mn_{0.2}Co_{0.2}O_2$) and NMC811 ($LiNi_{0.8}Mn_{0.1}Co_{0.1}O_2$) were obtained from ECOPRO, South Korea. The pristine particles of NMC622 and 811 are around 7 μm, shown by scanning electron microscopy (SEM) in our previous characterizations,[50] rendering the comparison between them in this study very fair. Moreover, the pristine materials are free of impurities, as shown in X-ray diffraction (XRD) in Figure S14. In this study, we employed oxide-only electrodes since using composite electrodes introduces the complexity of oxygenated species from the binder and carbon upon charge, where inclusion of the binder and carbon might introduce difficulty in the interpretation of the data through forming oxygen-containing parasitic products at high potentials, which could

affect the O K-edge XAS spectra. The pellet electrode was prepared through pelletizing around 48 mg of active materials using 6 mm diameter pressing die set (Across International) for 15 min. The pellets were then sintered under oxygen flow at 750 and 725 °C for 6 h, for NMC622 and 811, respectively. The cooling and heating rates are controlled to be 2 °C/min. The pellet electrodes are then broken into pieces of around 3 mg each, then dry in vacuum under 120 °C overnight before transferred into an argon-filled glovebox (<0.5 ppm of H_2O and O_2). The oxide-only electrode has very comparable electrochemistry profile to composite electrode[3,4] when cycling to 4.8 V_{Li} and discharge back to 2 V_{Li}, as shown in Figure S15.

4.2. Electrochemistry. Electrochemical behavior of the electrodes was confirmed by galvanostatic measurements in two-electrode cells (Tomcell type TJ-AC). Cells were assembled in an argon-filled glovebox (<0.5 ppm of H_2O and O_2) and comprised a lithium metal foil as the negative electrode and the positive electrode, separated by two pieces of the polypropylene separator (2500 Celgard), impregnated with 150 μL of different electrolytes including LP57 (1M $LiPF_6$ in a 3:7 ethylene carbonate (EC): ethylmethyl carbonate (EMC) electrolyte (BASF)). After assembly, the cells rested for 6 h prior to measurement and then were charged with different end-of-charge potentials (4.1, 4.2, 4.4, 4.6, and 4.8 V_{Li}) at a C/100 rate (2.8 mA/g), based on the theoretical capacity calculated assuming full delithiation. The cells were maintained at the end-of-charge potential for 5 h before disassembly in the glovebox. For the charged pellet electrode, they were rinsed in 1 mL of EMC solution with stirring for 24 h to remove the residual electrolyte and electrolyte decomposition products on the surface. The pellets were then dried in vacuum for 4 h before further characterization using XAS.

4.3. Synchrotron Measurements. Transition-metal L-edges and O K-edge XAS were conducted in Canadian Light Source (CLS) beamline 10 ID-2 on the charged pellets and transition-metal K-edges XAS were conducted at the Stanford Synchrotron Radiation Lightsource (SSRL) at the SLAC National Accelerator Laboratory, Beamline 6-2b in transmission mode with an active material mass fraction of 10%, diluted with sucrose, using a Si(111) analyzer. The soft X-ray XAS measurement is aligned with TiO_2 reference. The hard X-ray spectra are aligned using the Si(111) glitches. All spectroscopy data were normalized and processed using the ATHENA software package.[39] For O K-edge and transition-metal K-edge XAS, the spectra were normalized by reducing the pre-edge to intensity of 0 and the continuum after the whiteline to intensity of 1. The metal L-edge spectra were background-subtracted by fitting a polynomial, and the maxima was normalized to 1. The edge onset energies for Co are extracted by linear extrapolating the energy at 0.5 of the maximum of the intensity of the XAS spectra, whereas for Mn the edge onset energies are extracted by extrapolating the energy at 0.2 of the maximum of the intensity the XAS spectra due to the low-energy shoulder of the spectra. For soft X-ray measurement, the samples are sealed inside the argon-filled glovebox in the aluminum foil bag before transfer into the XAS chamber. While mounting the sample holder to the XAS chamber, there is a certain period of exposure in air, which is minimized down to less than 5 s. We believe what we have observed in XAS TEY is not affected by such a short time of exposure to air as there is no obvious signal of air exposure products[36] such as LiOH[51] and Li_2CO_3[37] in O K-edge TEY in the charged oxides. Furthermore, there is a very consistent trend observed in Ni L-edge in terms of Ni oxidation and very comparable with previous literature reports in similar chemistries.[16] The TFY data is definitely not affected by such short exposure considering the probing length scale is around 100 nm. Furthermore, TFY of 3d metal L-edge suffers from self-absorption issues, and this could be alleviated by using the inverse partial fluorescence yield (iPFY), which is the inversed intensity of O Kα emission in the RIXS.[52] iPFY mode is partially eliminated with obvious self-absorption and line distortion.[53] As shown in Figure S16, S17, iPFY shows very consistent trend with the TFY data even though with different doublet ratios for Ni due to the line distortion and saturation in TFY. However, we still keep the TFY information in the main text and iPFY in the Supporting Information because TFY is much more widely used in the literature,[14,16,17] which allows us to compare with literature data,[14,16,17] as shown in Figure 3.

AUTHOR INFORMATION

Corresponding Authors

Yang Yu − *Department of Materials Science and Engineering, MIT, Cambridge, Massachusetts 02139, United States*; Email: yuy@mit.edu

Yang Shao-Horn − *Department of Materials Science and Engineering, Department of Mechanical Engineering, and Research Laboratory of Electronics, MIT, Cambridge, Massachusetts 02139, United States*; orcid.org/0000-0001-8714-2121; Email: shaohorn@mit.edu

Authors

Pinar Karayaylali − *Department of Mechanical Engineering, MIT, Cambridge, Massachusetts 02139, United States*

Livia Giordano − *Department of Mechanical Engineering, MIT, Cambridge, Massachusetts 02139, United States*; orcid.org/0000-0002-6879-9424

Juan Corchado-García − *Research Laboratory of Electronics, MIT, Cambridge, Massachusetts 02139, United States*

Jonathan Hwang − *Department of Materials Science and Engineering, MIT, Cambridge, Massachusetts 02139, United States*

Dimosthenis Sokaras − *SLAC National Accelerator Laboratory, Menlo Park, California 94025, United States*

Filippo Maglia − *BMW Group, 80788 München, Germany*

Roland Jung − *BMW Group, 80788 München, Germany*; orcid.org/0000-0003-1135-7438

Forrest S. Gittleson − *BMW Group Technology Office USA, Mountain View, California 94043, United States*

Notes

The authors declare no competing financial interest.

ACKNOWLEDGMENTS

Research at MIT related to this work was supported financially by BMW. Part or all of the research described in this paper was performed at the Canadian Light Source, a national research facility of the University of Saskatchewan, which is supported by the Canada Foundation for Innovation (CFI), the Natural Sciences and Engineering Research Council (NSERC), the National Research Council (NRC), the Canadian Institutes of Health Research (CIHR), the Government of Saskatchewan, and the University of Saskatchewan. Use of the Stanford Synchrotron Radiation Lightsource (SSRL), SLAC National Accelerator Laboratory, was supported by the US Department of Energy, Office of Science, Office of Basic Energy Sciences (contract No. DE-AC02-76SF00515). Part of the instrument used for this study was supported by the U.S. Department of Energy, Office of Energy Efficiency & Renewable Energy, Solar

Energy Technology Office BRIDGE Program. This research used resources of the National Energy Research Scientific Computing Center (NERSC), a DOE Office of Science User Facility supported by the Office of Science of the U.S. Department of Energy under Contract No. DE-AC02-05CH11231. This work also used resources of the Extreme Science and Engineering Discovery Environment (XSEDE), which is supported by National Science Foundation grant number ACI-1548562. We thank Dr. Teak Boyko for the useful discussion on processing the inverse partial fluorescence yield data.

REFERENCES

(1) Lu, Z.; MacNeil, D.; Dahn, J. Layered $Li[Ni_xCo_{1-2x}Mn_x]O_2$ Cathode Materials for Lithium-Ion Batteries. *Electrochem. Solid-State Lett.* **2001**, *4*, A200−A203.

(2) Noh, H.-J.; Youn, S.; Yoon, C. S.; Sun, Y.-K. Comparison of the Structural and Electrochemical Properties of Layered $Li[Ni_xCo_yMn_z]O_2$ (X = 1/3, 0.5, 0.6, 0.7, 0.8 and 0.85) Cathode Material for Lithium-Ion Batteries. *J. Power Sources* **2013**, *233*, 121−130.

(3) Jung, R.; Metzger, M.; Maglia, F.; Stinner, C.; Gasteiger, H. A. Oxygen Release and Its Effect on the Cycling Stability of LiNixMnyCozO2 (NMC) Cathode Materials for Li-Ion Batteries. *J. Electrochem. Soc.* **2017**, *164*, A1361−A1377.

(4) Jung, R.; Metzger, M.; Maglia, F.; Stinner, C.; Gasteiger, H. A. Chemical versus Electrochemical Electrolyte Oxidation on NMC111, NMC622, NMC811, LNMO, and Conductive Carbon. *J. Phys. Chem. Lett.* **2017**, *8*, 4820−4825.

(5) Yu, Y.; Karayaylali, P.; Katayama, Y.; Giordano, L.; Gauthier, M.; Maglia, F.; Jung, R.; Lund, I.; Shao-Horn, Y. Coupled LiPF6 Decomposition and Carbonate Dehydrogenation Enhanced by Highly Covalent Metal Oxides in High-Energy Li-Ion Batteries. *J. Phys. Chem. C* **2018**, *122*, 27368−27382.

(6) Zhang, N.; Li, J.; Li, H.; Liu, A.; Huang, Q.; Ma, L.; Li, Y.; Dahn, J. R. Structural, Electrochemical, and Thermal Properties of Nickel-Rich $LiNi_xMn_yCo_zO_2$ Materials. *Chem. Mater.* **2018**, *30*, 8852−8860.

(7) Karayaylali, P.; Tatara, R.; Zhang, Y.; Chan, K.-L.; Yu, Y.; Giordano, L.; Maglia, F.; Jung, R.; Lund, I.; Shao-Horn, Y. Coating-Dependent Electrode-Electrolyte Interface for Ni-Rich Positive Electrodes in Li-Ion Batteries. *J. Electrochem. Soc.* **2019**, *166*, A1022−A1030.

(8) Zhang, Y.; Katayama, Y.; Tatara, R.; Giordano, L.; Yu, Y.; Fraggedakis, D.; Sun, J. G.; Maglia, F.; Jung, R.; Bazant, M. Z.; Shao-Horn, Y. Revealing Electrolyte Oxidation via Carbonate Dehydrogenation on Ni-Based Oxides in Li-Ion Batteries by in Situ Fourier Transform Infrared Spectroscopy. *Energy Environ. Sci.* **2020**, *13*, 183−199.

(9) Giordano, L.; Karayaylali, P.; Yu, Y.; Katayama, Y.; Maglia, F.; Lux, S.; Shao-Horn, Y. Chemical Reactivity Descriptor for the Oxide-Electrolyte Interface in Li-Ion Batteries. *J. Phys. Chem. Lett.* **2017**, *8*, 3881−3887.

(10) Ceder, G.; Aydinol, M. K.; Kohan, A. F. Application of First-Principles Calculations to the Design of Rechargeable Li-Batteries. *Comput. Mater. Sci.* **1997**, *8*, 161−169.

(11) Ceder, G.; Chiang, Y.-M.; Sadoway, D. R.; Aydinol, M. K.; Jang, Y.-I.; Huang, B. Identification of Cathode Materials for Lithium Batteries Guided by First-Principles Calculations. *Nature* **1998**, *392*, 694−696.

(12) Goodenough, J. B.; Kim, Y. Challenges for Rechargeable Li Batteries. *Chem. Mater.* **2010**, *22*, 587−603.

(13) Mansour, A. N.; Croguennec, L.; Prado, G.; Delmas, C. In Situ XAS Study of LixNi0. 7Fe0. 15Co0. 15O2 Cathode Material. *J. Synchrotron Radiat.* **2001**, *8*, 866−868.

(14) Tian, C.; Nordlund, D.; Xin, H. L.; Xu, Y.; Liu, Y.; Sokaras, D.; Lin, F.; Doeff, M. M. Depth-Dependent Redox Behavior of LiNi0. 6Mn0. 2Co0. 2O2. *J. Electrochem. Soc.* **2018**, *165*, A696−A704.

(15) Kondrakov, A. O.; Geßwein, H.; Galdina, K.; De Biasi, L.; Meded, V.; Filatova, E. O.; Schumacher, G.; Wenzel, W.; Hartmann, P.; Brezesinski, T.; Janek, J. Charge-Transfer-Induced Lattice Collapse in Ni-Rich NCM Cathode Materials during Delithiation. *J. Phys. Chem. C* **2017**, *121*, 24381−24388.

(16) Li, N.; Sallis, S.; Papp, J. K.; Wei, J.; McCloskey, B. D.; Yang, W.; Tong, W. Unraveling the Cationic and Anionic Redox Reactions in a Conventional Layered Oxide Cathode. *ACS Energy Lett.* **2019**, *4*, 2836−2842.

(17) Lin, F.; Markus, I. M.; Nordlund, D.; Weng, T.-C.; Asta, M. D.; Xin, H. L.; Doeff, M. M. Surface Reconstruction and Chemical Evolution of Stoichiometric Layered Cathode Materials for Lithium-Ion Batteries. *Nat. Commun.* **2014**, *5*, No. 3529.

(18) Mu, L.; Kan, W. H.; Kuai, C.; Yang, Z.; Li, L.; Sun, C.-J.; Sainio, S.; Avdeev, M.; Nordlund, D.; Lin, F. Structural and Electrochemical Impacts of Mg/Mn Dual Dopants on the LiNiO2 Cathode in Li-Metal Batteries. *ACS Appl. Mater. Interfaces* **2020**, *12*, 12874−12882.

(19) Li, J.; Liu, H.; Xia, J.; Cameron, A. R.; Nie, M.; Botton, G. A.; Dahn, J. The Impact of Electrolyte Additives and Upper Cut-off Voltage on the Formation of a Rocksalt Surface Layer in LiNi0. 8Mn0. 1Co0. 1O2 Electrodes. *J. Electrochem. Soc.* **2017**, *164*, A655.

(20) Liu, H.; Bugnet, M.; Tessaro, M. Z.; Harris, K. J.; Dunham, M. J.; Jiang, M.; Goward, G. R.; Botton, G. A. Spatially Resolved Surface Valence Gradient and Structural Transformation of Lithium Transition Metal Oxides in Lithium-Ion Batteries. *Phys. Chem. Chem. Phys.* **2016**, *18*, 29064−29075.

(21) de Groot, F. M.; Hu, Z.; López, M. F.; Kaindl, G.; Guillot, F.; Tronc, M. Differences between L 3 and L 2 X-Ray Absorption Spectra of Transition Metal Compounds. *J. Chem. Phys.* **1994**, *101*, 6570−6576.

(22) Cramer, S. P.; DeGroot, F. M. F.; Ma, Y.; Chen, C. T.; Sette, F.; Kipke, C. A.; Eichhorn, D. M.; Chan, M. K.; Armstrong, W. H.; et al. Ligand Field Strengths and Oxidation States from Manganese L-Edge Spectroscopy. *J. Am. Chem. Soc.* **1991**, *113*, 7937−7940.

(23) Zheng, X.; Zhang, B.; De Luna, P.; Liang, Y.; Comin, R.; Voznyy, O.; Han, L.; de Arquer, F. P. G.; Liu, M.; Dinh, C. T.; et al. Theory-Driven Design of High-Valence Metal Sites for Water Oxidation Confirmed Using in Situ Soft X-Ray Absorption. *Nat. Chem.* **2018**, *10*, 149.

(24) Stavitski, E.; De Groot, F. M. The CTM4XAS Program for EELS and XAS Spectral Shape Analysis of Transition Metal L Edges. *Micron* **2010**, *41*, 687−694.

(25) Gilmore, K.; Vinson, J.; Shirley, E. L.; Prendergast, D.; Pemmaraju, C. D.; Kas, J. J.; Vila, F. D.; Rehr, J. J. Efficient Implementation of Core-Excitation Bethe−Salpeter Equation Calculations. *Comput. Phys. Commun.* **2015**, *197*, 109−117.

(26) Yu, Y.; Karayaylali, P.; Nowak, S. H.; Giordano, L.; Gauthier, M.; Hong, W.; Kou, R.; Li, Q.; Vinson, J.; Kroll, T.; et al. Revealing Electronic Signatures of Lattice Oxygen Redox in Lithium Ruthenates and Implications for High-Energy Li-Ion Battery Material Designs. *Chem. Mater.* **2019**, *31*, 7864−7876.

(27) Yano, M.; Suzuki, S.; Miyayama, M.; Ohgaki, M. Electrochemical Properties of Layer-Structured $H_x(Ni_{1/3}Co_{1/3}Mn_{1/3})O_2$ for Electrochemical Capacitors in Alkaline Aqueous Solutions. *J. Asian Ceram. Soc.* **2013**, *1*, 71−76.

(28) Suntivich, J.; Hong, W. T.; Lee, Y.-L.; Rondinelli, J. M.; Yang, W.; Goodenough, J. B.; Dabrowski, B.; Freeland, J. W.; Shao-Horn, Y. Estimating Hybridization of Transition Metal and Oxygen States in Perovskites from O K-Edge X-Ray Absorption Spectroscopy. *J. Phys. Chem. C* **2014**, *118*, 1856−1863.

(29) Qiao, R.; Roychoudhury, S.; Zhuo, Z.; Li, Q.; Lyu, Y.; Kim, J.-H.; Liu, J.; Lee, E.; Polzin, B. J.; Guo, J. *Deciphering the Oxygen Absorption Pre-Edge: Universal Map of Transition Metal Redox Potentials in Batteries*, 2019.

(30) Kuznetsov, D. A.; Han, B.; Yu, Y.; Rao, R. R.; Hwang, J.; Román-Leshkov, Y.; Shao-Horn, Y. Tuning Redox Transitions via Inductive Effect in Metal Oxides and Complexes, and Implications in Oxygen Electrocatalysis. *Joule* **2018**, *2*, 225−244.

(31) Renfrew, S. E.; McCloskey, B. D. Residual Lithium Carbonate Predominantly Accounts for First Cycle CO2 and CO Outgassing of

Li-Stoichiometric and Li-Rich Layered Transition-Metal Oxides. *J. Am. Chem. Soc.* **2017**, *139*, 17853−17860.
(32) Renfrew, S. E.; McCloskey, B. D. Quantification of Surface Oxygen Depletion and Solid Carbonate Evolution on the First Cycle of LiNi0. 6Mn0. 2Co0. 2O2 Electrodes. *ACS Appl. Energy Mater.* **2019**, *2*, 3762−3772.
(33) Renfrew, S. E.; Kaufman, L. A.; McCloskey, B. D. Altering Surface Contaminants and Defects Influences the First-Cycle Outgassing and Irreversible Transformations of LiNi0. 6Mn0. 2Co0. 2O2. *ACS Appl. Mater. Interfaces* **2019**, *11*, 34913−34921.
(34) Hong, W. T.; Stoerzinger, K. A.; Moritz, B.; Devereaux, T. P.; Yang, W.; Shao-Horn, Y. Probing LaMO3 Metal and Oxygen Partial Density of States Using X-Ray Emission, Absorption, and Photoelectron Spectroscopy. *J. Phys. Chem. C* **2015**, *119*, 2063−2072.
(35) Qiao, R.; Liu, J.; Kourtakis, K.; Roelofs, M. G.; Peterson, D. L.; Duff, J. P.; Deibler, D. T.; Wray, L. A.; Yang, W. Transition-Metal Redox Evolution in LiNi0. 5Mn0. 3Co0. 2O2 Electrodes at High Potentials. *J. Power Sources* **2017**, *360*, 294−300.
(36) Jung, R.; Morasch, R.; Karayaylali, P.; Phillips, K.; Maglia, F.; Stinner, C.; Shao-Horn, Y.; Gasteiger, H. A. Effect of Ambient Storage on the Degradation of Ni-Rich Positive Electrode Materials (NMC811) for Li-Ion Batteries. *J. Electrochem. Soc.* **2018**, *165*, A132−A141.
(37) Qiao, R.; Chuang, Y.-D.; Yan, S.; Yang, W. Soft X-Ray Irradiation Effects of Li2O2, Li2CO3 and Li2O Revealed by Absorption Spectroscopy. *PLoS One* **2012**, *7*, No. e49182.
(38) Xu, Y.; Hu, E.; Zhang, K.; Wang, X.; Borzenets, V.; Sun, Z.; Pianetta, P.; Yu, X.; Liu, Y.; Yang, X.-Q.; et al. In Situ Visualization of State-of-Charge Heterogeneity within a LiCoO2 Particle That Evolves upon Cycling at Different Rates. *ACS Energy Letters* **2017**, *2*, 1240−1245.
(39) Ravel, B.; Newville, M. ATHENA, ARTEMIS, HEPHAESTUS: Data Analysis for X-Ray Absorption Spectroscopy Using IFEFFIT. *J. Synchrotron Radiat.* **2005**, *12*, 537−541.
(40) Yamamoto, T. Assignment of Pre-Edge Peaks in K-Edge x-Ray Absorption Spectra of 3d Transition Metal Compounds: Electric Dipole or Quadrupole? *X-Ray Spectrom.* **2008**, *37*, 572−584.
(41) Risch, M.; Stoerzinger, K. A.; Han, B.; Regier, T. Z.; Peak, D.; Sayed, S. Y.; Wei, C.; Xu, Z.; Shao-Horn, Y. Redox Processes of Manganese Oxide in Catalyzing Oxygen Evolution and Reduction: An in Situ Soft X-Ray Absorption Spectroscopy Study. *J. Phys. Chem. C* **2017**, *121*, 17682−17692.
(42) Grimaud, A.; Carlton, C. E.; Risch, M.; Hong, W. T.; May, K. J.; Shao-Horn, Y. Oxygen Evolution Activity and Stability of Ba6Mn5O16, Sr4Mn2CoO9, and Sr6Co5O15: The Influence of Transition Metal Coordination. *J. Phys. Chem. C* **2013**, *117*, 25926−25932.
(43) Vura-Weis, J.; Jiang, C.-M.; Liu, C.; Gao, H.; Lucas, J. M.; De Groot, F. M.; Yang, P.; Alivisatos, A. P.; Leone, S. R. Femtosecond M2, 3-Edge Spectroscopy of Transition-Metal Oxides: Photoinduced Oxidation State Change in α-Fe2O3. *J. Phys. Chem. Lett.* **2013**, *4*, 3667−3671.
(44) Nayak, P. K.; Grinblat, J.; Levi, M.; Wu, Y.; Powell, B.; Aurbach, D. TEM and Raman Spectroscopy Evidence of Layered to Spinel Phase Transformation in Layered LiNi1/3Mn1/3Co1/3O2 upon Cycling to Higher Voltages. *J. Electroanal. Chem.* **2014**, *733*, 6−19.
(45) Yoon, W.-S.; Kim, K.-B.; Kim, M.-G.; Lee, M.-K.; Shin, H.-J.; Lee, J.-M.; Lee, J.-S.; Yo, C.-H. Oxygen Contribution on Li-Ion Intercalation− Deintercalation in LiCoO2 Investigated by O K-Edge and Co L-Edge X-Ray Absorption Spectroscopy. *J. Phys. Chem. B* **2002**, *106*, 2526−2532.
(46) Schipper, F.; Erickson, E. M.; Erk, C.; Shin, J.-Y.; Chesneau, F. F.; Aurbach, D. Recent Advances and Remaining Challenges for Lithium Ion Battery Cathodes I. Nickel-Rich, LiNixCoyMnzO2. *J. Electrochem. Soc.* **2017**, *164*, A6220−A6228.
(47) Wandt, J.; Freiberg, A. T.; Ogrodnik, A.; Gasteiger, H. A. Singlet Oxygen Evolution from Layered Transition Metal Oxide Cathode Materials and Its Implications for Lithium-Ion Batteries. *Mater. Today* **2018**, *21*, 825−833.
(48) Ryu, H.-H.; Park, G.-T.; Yoon, C. S.; Sun, Y.-K. Suppressing Detrimental Phase Transitions via Tungsten Doping of LiNiO 2 Cathode for Next-Generation Lithium-Ion. *J. Mater. Chem. A* **2019**, *7*, 18580−18588.
(49) Tatara, R.; Yu, Y.; Karayaylali, P.; Chan, A. K.; Zhang, Y.; Jung, R.; Maglia, F.; Giordano, L.; Shao-Horn, Y. Enhanced Cycling Performance of Ni-Rich Positive Electrodes (NMC) in Li-Ion Batteries by Reducing Electrolyte Free-Solvent Activity. *ACS Appl. Mater. Interfaces* **2019**, *11*, 34973−34988.
(50) Zhang, Y.; Katayama, Y.; Tatara, R.; Giordano, L.; Yu, Y.; Fraggedakis, D.; Sun, J. G.; Maglia, F.; Jung, R.; Bazant, M. Z.; et al. Revealing Electrolyte Oxidation via Carbonate Dehydrogenation on Ni-Based Oxides in Li-Ion Batteries by in Situ Fourier Transform Infrared Spectroscopy. *Energy Environ. Sci.* **2020**, *13*, 183−189.
(51) Qiao, R.; Lucas, I. T.; Karim, A.; Syzdek, J.; Liu, X.; Chen, W.; Persson, K.; Kostecki, R.; Yang, W. Distinct Solid-Electrolyte-Interphases on Sn (100) and (001) Electrodes Studied by Soft X-Ray Spectroscopy. *Adv. Mater. Interfaces* **2014**, *1*, No. 1300115.
(52) Wadati, H.; Achkar, A.; Hawthorn, D.; Regier, T.; Singh, M.; Truong, K.; Fournier, P.; Chen, G.; Mizokawa, T.; Sawatzky, G. Utility of the Inverse Partial Fluorescence for Electronic Structure Studies of Battery Materials. *Appl. Phys. Lett.* **2012**, *100*, No. 193906.
(53) Asakura, D.; Hosono, E.; Nanba, Y.; Zhou, H.; Okabayashi, J.; Ban, C.; Glans, P.-A.; Guo, J.; Mizokawa, T.; Chen, G.; et al. Material/Element-Dependent Fluorescence-Yield Modes on Soft X-Ray Absorption Spectroscopy of Cathode Materials for Li-Ion Batteries. *AIP Adv.* **2016**, *6*, No. 035105.